Supporting Information

Systematic Evaluation of Lithium-excess Polyanionic Compounds as Multi-electron Reaction Cathodes

*Ruhong Li [a], Jianchao Liu [a], Tianrui Chen [a], Changsong Dai * [a], Ningyi Jiang * [b]*

[a] MIIT Key Laboratory of Critical Materials Technology for New Energy Conversion and Storage, School of Chemistry and Chemical Engineering, Harbin Institute of Technology, Harbin 150001, P.R. China.

[b] Tianjin Space Power Technology Co., Ltd., Tianjin Institute of Power Sources, Tianjin 300381, P.R. China

Experimental

1 Materials Preparation

All samples were synthesized by a modified solid-state reaction combining a simple ball-milling and a subsequent annealing treatment. The mixture containing various stoichiometric amounts of LiOH, V_2O_5, $NH_4H_2PO_4$ and sucrose were ball-milled for 7 h at a rotation rate of 200 revolutions per minute.The Li :V: P ratios were seted to (3+3*x*):(2-*x*):3, where *x*=0, 0.10, 0.15, 0.20 and 0.30. The presursors were then heated at 700, 750 and 800 °C for 8 h under argon atmosphere with a ramping rate of 2 °C min^{-1}. After naturally cooling to room temperature, the final product was obtained.

2 Materials Characterization

The compositions of Li, V and P in the samples were determined by inductively coupled plasma optical emission spectrometry (ICP-OES, PerkinElmer Optima 5300DV, USA). The composition and chemical state were examined by X-ray Photoelectron spectroscopy (XPS, PHI 5700 ESCA System, USA). The binding energy scale was calibrated using the reference binding energy of C 1s peak at 284.8 eV. The residual carbon contents of pristine and Li-excess LVP composites were verified by thermogravimetric analysis (TGA) using simultaneous thermo-analyzer (ZRY-2P, China) at a heating rate of 5 ^oC /min from 25 ^oC to 800 ^oC. In order to measure electron conductivity of the synthesized LVPs, a certain amount of sample was placed in a mold and pressed into a round cake with pressure of 16 MPa, then the resistance of the pressed round cake was analyzed with a four-probe conductivity meter (Keithley Model 2400). The crystal structure of the materials was performed using X-ray powder diffraction (XRD, Rigaku, D/max–γβ X' pert diffractometer, Japan) with Cu Kα radiation, the scanning range of 10°–130° and step size 0.01°. Rietveld refinements of the X-ray powder diffraction patterns were carried out using the GSAS/EXPGUI package. The morphologies and particle sizes of the samples were observed with a scanning electron microscope (SEM, HITACHI S-4700, Japan) coupled with an energy dispersive spectrum X-ray detector (EDS) and transmission electron microscopy (TEM, JEM-2100). Li chemical states in the samples were performed by ^7Li Solid State Nuclear Magnetic Resonance (SSNMR, Bruker Avance III 400 spectrometer, USA) at magic angle spinning (MAS) frequencies of 30 kHz. The spectra were referenced to a 1 M aqueous solution of LiCl set at 0 ppm. The V L-edge and P L-edge X-ray absorption near edge structure (XANES) were measured in fluorescence mode at the XMCD beamline (BL12B), while the V K-edge spectra were measured in transmission mode at the U7C beamline of the National Synchrotron Radiation Laboratory (NSRL, Hefei, China).

3 Computational Details

3.1 Structural Optimization and Electronic structures

Our calculations were based on density functional theory as implemented in the Quantum ESPRESSO package [1, 2]. The generalized gradient approximation of Perdew, Burke and Ernzerhof was employed to the exchange and correlation functional. The electron wavefunctions and charge density were represented by a plane-wave basis set using an energy cutoff of 450 eV. To describe correctly the energetics of the V 3d states, Hubbard correction with U_{eff} = 3.25 eV was introduced in our calculations [3]. For defect calculations, we used a (2×1×1) supercell and a 3×3×3 k-point mesh. Convergence with respect to self-consistent iterations was assumed when the total energy difference between cycles was less than 10^{-5} eV and the residual forces were less than 0.01 eV/Å. The total and projected density of states were calculated for this optimized structure. 3D structural diagrams were plotted using the VESTA software (visualization for electronic and structural analysis) [4].

3.2 NMR chemical shift calculation

The NMR chemical shift calculations were performed with the CASTEP code implemented in the Materials Studio 6.0 environment, for the experimental and geometry optimized structures [5]. The core-valence interactions were described by ultra-soft pseudopotentials (USPP). The USPP were generated using the on the fly generator included in CASTEP. The wave functions were expanded on a plane-wave basis set with a kinetic energy cutoff of 600 eV. The Brillouin zone was sampled using a Monkhorst–Pack grid spacing with a k-point mesh of 4×4×4).

3.3 Lithium ion diffusion behaviors

3.3.1 Bond-valence energy landscape (BVEL) method

The bond-valence (BV) calculations are a well-established method of validating crystal structure, locating light elements, assigning charge distribution etc. The BVEL method combines both a scaling term to convert oxidation state mismatch to energy and a Columbic repulsion term [6]. The possible Li^+ percolation pathways for normal and Li-excess LVPs were calculated with the 3DBVSMAPPER software, with an isosurfaces value of -3.0 eV.

3.3.2 Molecular dynamics simulation

We used molecular dynamics (MD) method to simulate the lithium ion diffusion behaviors in LVP and lithium-excess LVP [7, 8]. A supercell of 8 formula units (2×2×2) was introduced to avoid the imaginary interaction between the unit cells in periodic boundary condition (PBC). The initial structures were statically relaxed and were set to an initial temperature of 298 K. The structures were then heated to targeted temperatures (500-1200 K) at a constant rate by velocity scaling over a time period of

2 ps. The NVT ensemble using a Nose-Hoover thermostat was adopted. The total time was set to 500 ps with a time step of 2 fs.

The mean square displacement (MSD) can be used to characterize the diffusion behavior of the system. As in previous studies, the diffusivity D can be calculated based on (1)

$$D = \frac{1}{6N\Delta t}\sum_{i=1}^{N}\left\langle \left| r_i(t+\Delta t) - r_i(t) \right|^2 \right\rangle_t \qquad (1)$$

where N is the total number of diffusion ions, $r_i(t)$ is the position of the i-th Li^+ at the time t, the diffusion coefficient D can be calculated based on the slope of the MSD curves. The activation energy barrier for Li^+ diffusion can be extracted from the diffusion coefficients at various temperatures according to Arrhenius equation.

The detailed analysis of atomic trajectories has been focused on the number density $\rho(r,t)$ and time-space correlation of number density as van Hove correlation functions $G(r,t)$ [8, 9]. The dynamics of a multi-component material with n different chemical species can be described by a number density functions:

$$\rho_i(r,t) = \sum_{k=1}^{N} \delta\left[r - r_{i,k}(t)\right] \qquad (2)$$

where r is an arbitrary position in the material, $r_{i,k}(t)$ is the position of kth atom of species i at time t, and N_i is the total number of atoms in species i.

The van Hove time-space correlation function can also be employed to describe the correlation of number density. This function can be separated as a 'self' part $G_s(r,t)$and a 'distinct' part $G_d(r,t)$ as the following:

$$G_s(\Delta r,\Delta t) = \frac{1}{N}\left\langle \sum_{k=1}^{N} \delta\left[\Delta r + r_{i,k}(0) - r_{i,k}(\Delta t)\right] \right\rangle \qquad (3)$$

$$G_d(\Delta r,\Delta t) = \frac{1}{N}\left\langle \sum_{k=1}^{N}\sum_{l=1\neq k}^{N} \delta\left[\Delta r + r_{i,k}(0) - r_{i,l}(\Delta t)\right] \right\rangle \qquad (4)$$

where $\delta()$ is the one-dimensional Dirac delta function. $r_i(t)$ denotes the position of the ith Li^+ ion at time t. For a given r and t, the self-part $Gs(r,t)$ or its transformed version $r^2Gs(r,t)$ is related to the probability of finding one atom after it travels a distance r after a time interval of t; the distinct-part $G_d(r,t)$ or its transformed version $r^2Gd(r,t)$ compares the positions of a particle to the position of another particle at different time and is related to the probability of finding atom j ($j \neq i$) with a distance r (compare to the position of atom i at t_0) after a time interval of t.

3.3.3 Nudged elastic band (NEB) calculation

We used NEB method to determine the activation barrier of lithium ion diffusion in LVP and lithium-excess LVP [10, 11]. A supercell of 8 formula units was introduced to avoid the imaginary interaction between the unit cells in periodic boundary condition (PBC). Before NEB calculations, we performed a full geometric relaxation of LVP with free lattice parameters and internal degrees of freedom. Then, a single lithium vacancy was generated to describe the lithium vacancy diffusion in each supercell. After setting initial and final images, NEB calculations with 4 intermediate images were conducted with fixed lattice parameters and free internal degrees of freedom. To avoid the drift of images by the fake force, we fixed lattice parameters during NEB calculations. Since the lattice parameters were optimized before the NEB calculations, we believe that the errors caused by fixed lattice constants during NEB calculations are negligible, resulting in limited amount of errors on the NEB barriers. The calculations with an energy cutoff of 400 eV and a single *k*-point were performed until the free energy converges within 0.05 eV per unit cell.

4 Electrochemical Measurements

The CR2032-type coin cells were assembled to test the electrochemical properties with lithium foil as the anode and Celgard-2320 membrane as the separator. The electrolyte was composed of 1 M $LiPF_6$ dissolved in ethylene carbonate (EC), dimethyl carbonate (DMC) and diethyl carbonate (DEC) at a volumetric ratio of 1:1:1. All operations were done in an Ar-filled glovebox. Galvanostatic discharge–charge experiments were performed at different current densities with a multichannel battery tester (NEWWARE, China). The galvanostatic intermittent titration technique (GITT) test were performed at 0.1C rate with a relaxing time of 30 min. Cyclic voltammetry (CV) and electrochemical impedance spectra (EIS) were measured by the electrochemical workstation (CHI660E, Chenhua, China).

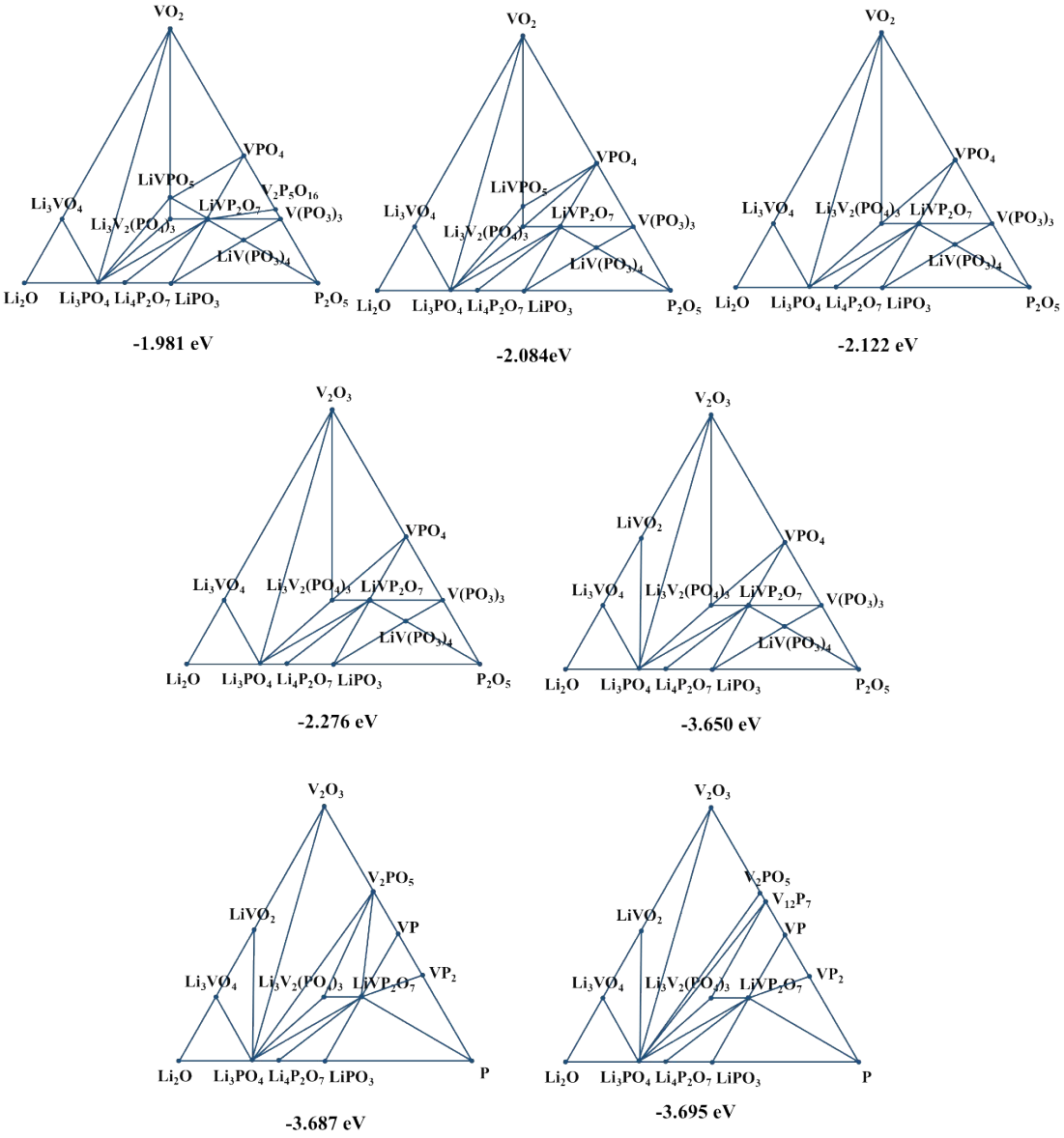

Figure S1 Phase diagrams under various μ_O ranging from -1.981 to -3.695 eV

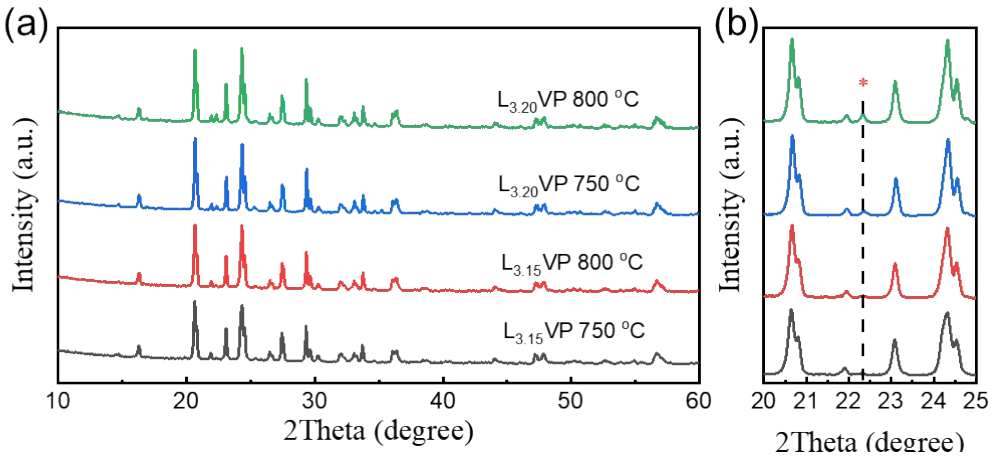

Table S2 XRD patterns of LVPs obtained under different temperatures

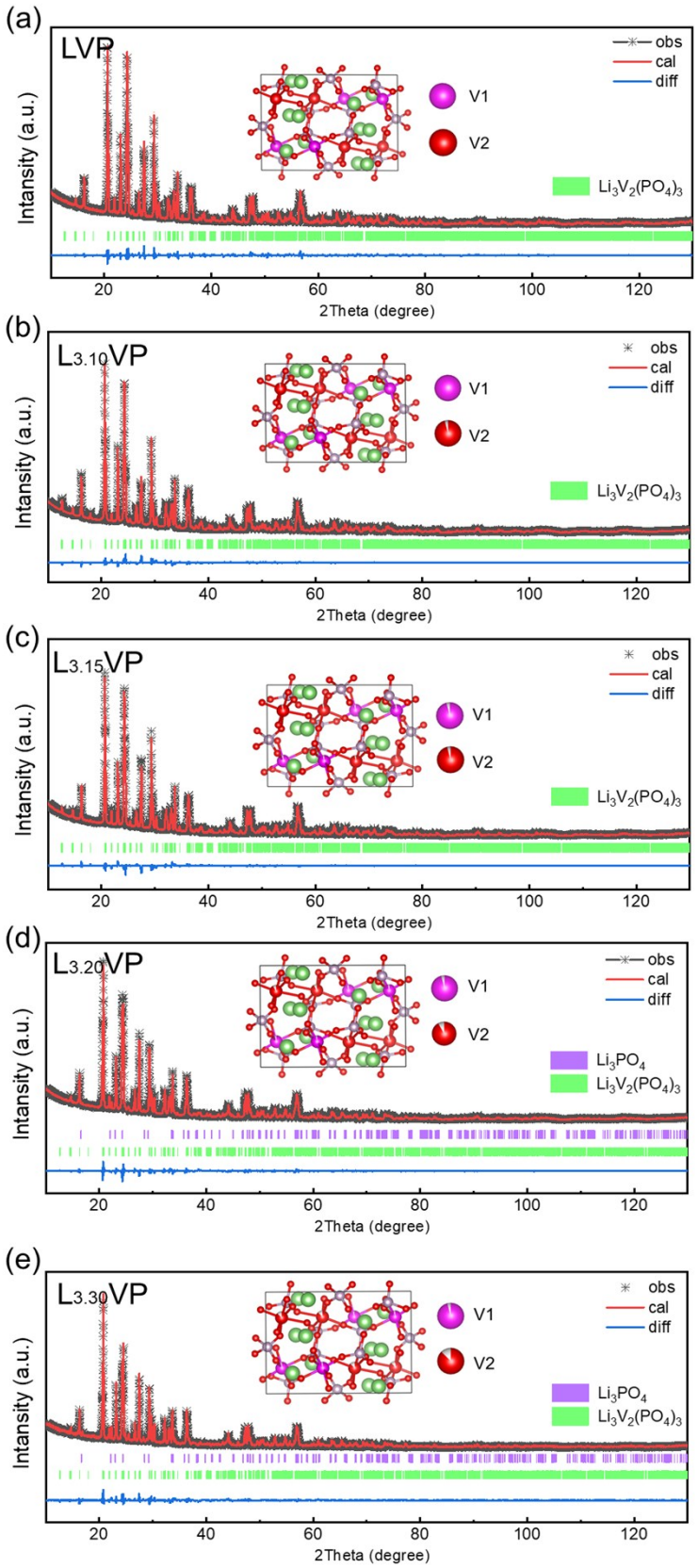

Figure S3 XRD Rietveld plots of LVP (a), $L_{3.10}VP$ (b), $L_{3.15}VP$ (c), $L_{3.20}VP$ (d) and $L_{3.30}VP$ (e)

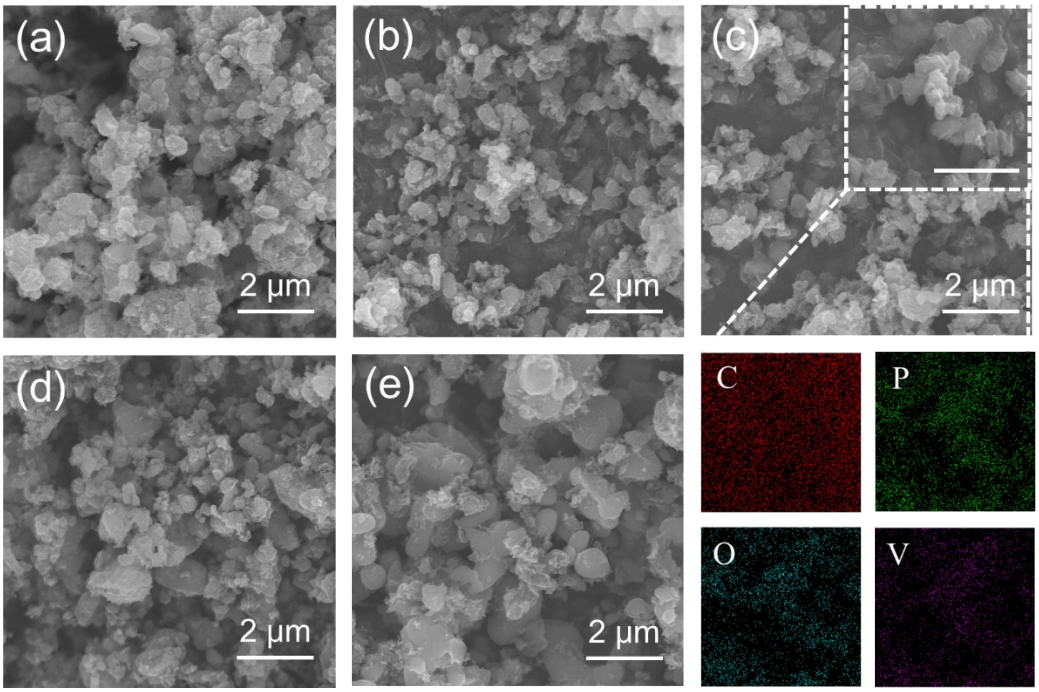

Figure S4 SEM images of various L_xVPs: (a) normal LVP, (b) $L_{3.10}$VP, (c) $L_{3.15}$VP, (d) $L_{3.20}$VP, (e) $L_{3.30}$VP. EDS elemental mapping of area in the insert of (c)

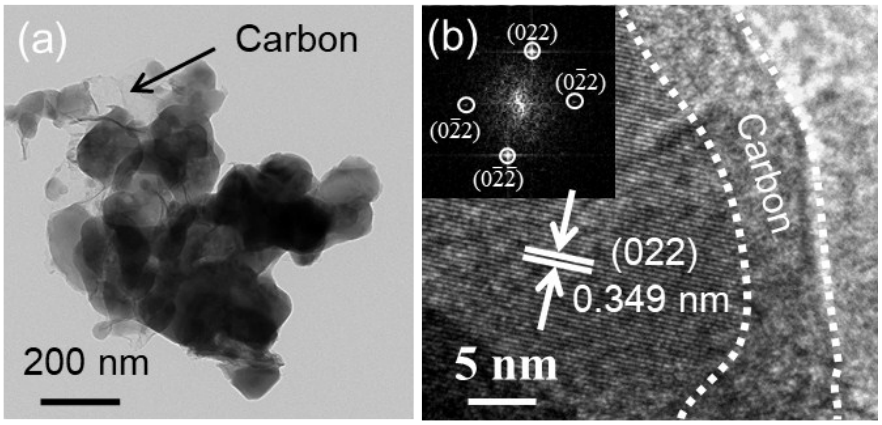

Figure S5 TEM (a) and HRTEM (b) images of normal LVP

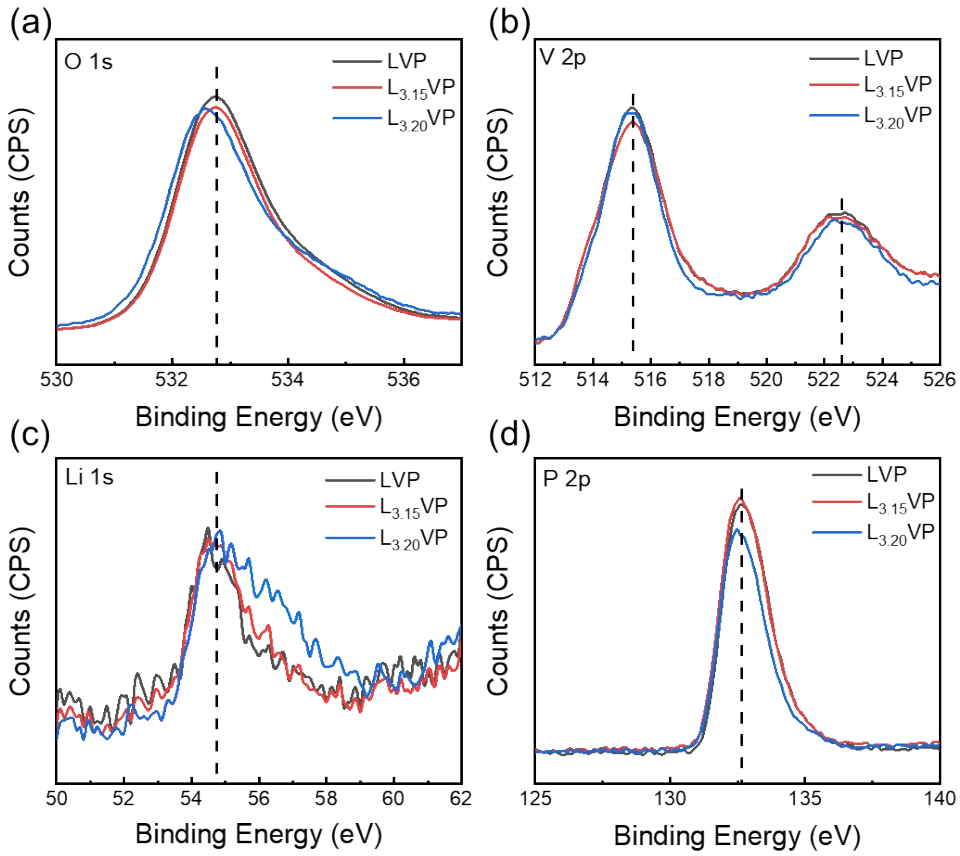

Figure S6 XPS results of LVP, $L_{3.15}VP$ and $L_{3.20}VP$: (a) O 1s, (b) V 2p, (c) Li 1s and (d) P 2p.

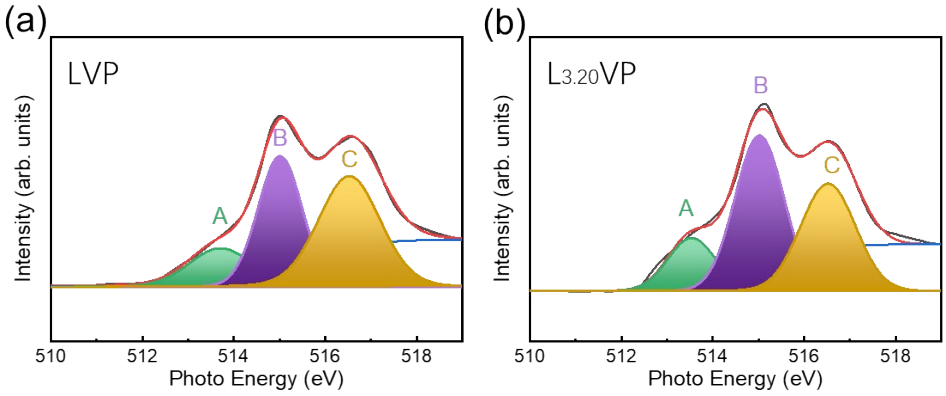

Figure S7. V L3-edge XAS for LVP and $L_{3.20}VP$

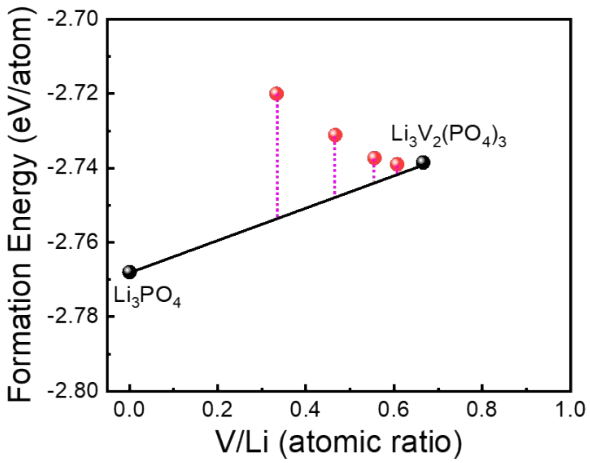

Figure S8. Formation energy of Li-excess LVPs

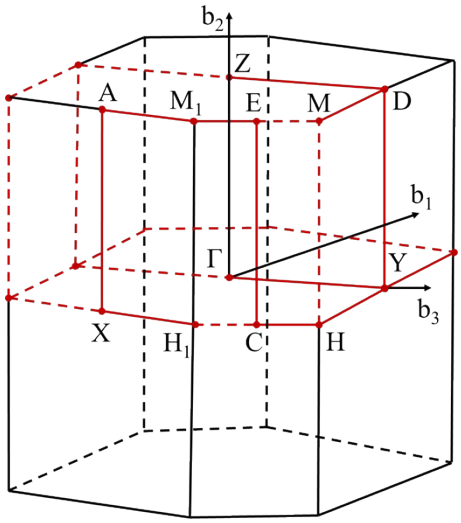

Figure S9 Brillouin zone of $Li_3V_2(PO_4)_3$ (monoclinic crystal structure) with high-symmetry *k*-points

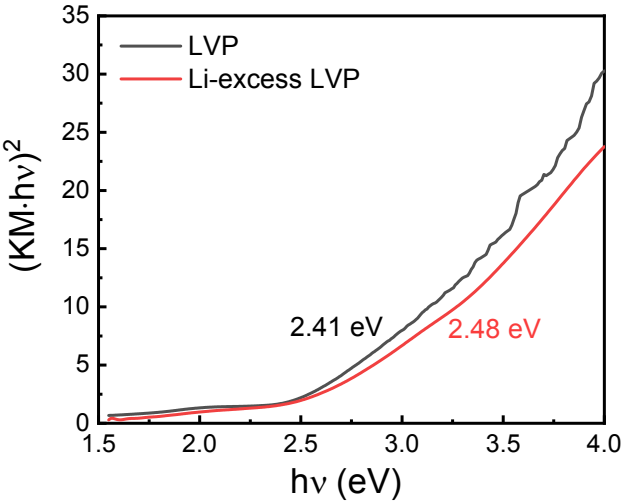

Figure S10 UV-vis spectra of normal LVP and Li-excess LVP

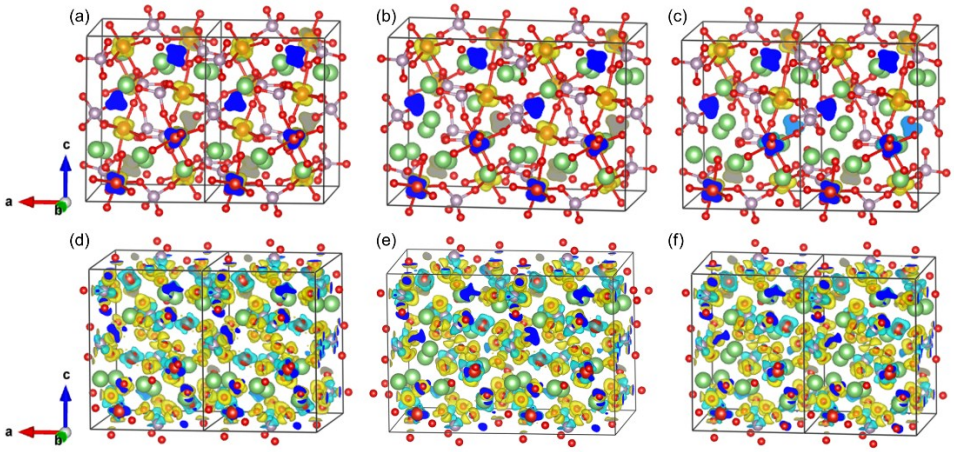

Figure S11 Spin-polarized charge density (a-c) and deformation charge density (d-f) for $Li_{24}V_{16}P_{24}O_{96}$, $Li_{27}V_{15}P_{24}O_{96}$ and $Li_{30}V_{14}P_{24}O_{96}$, espectively.

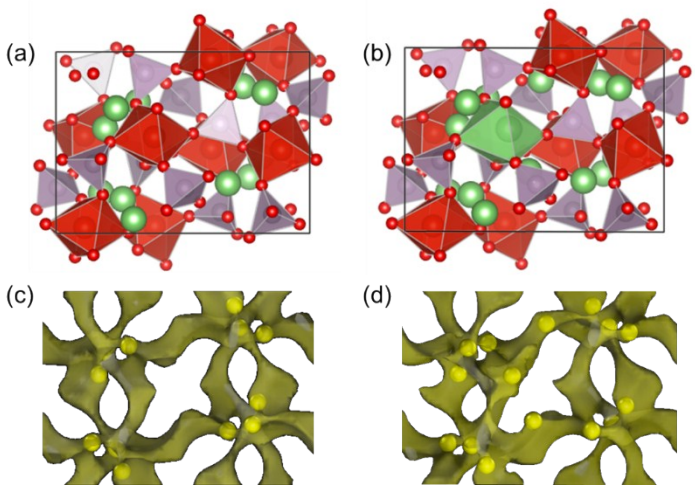

Figure S12 Lithium ion penetration paths for normal and Li-excess LVPs based on BVEL method.

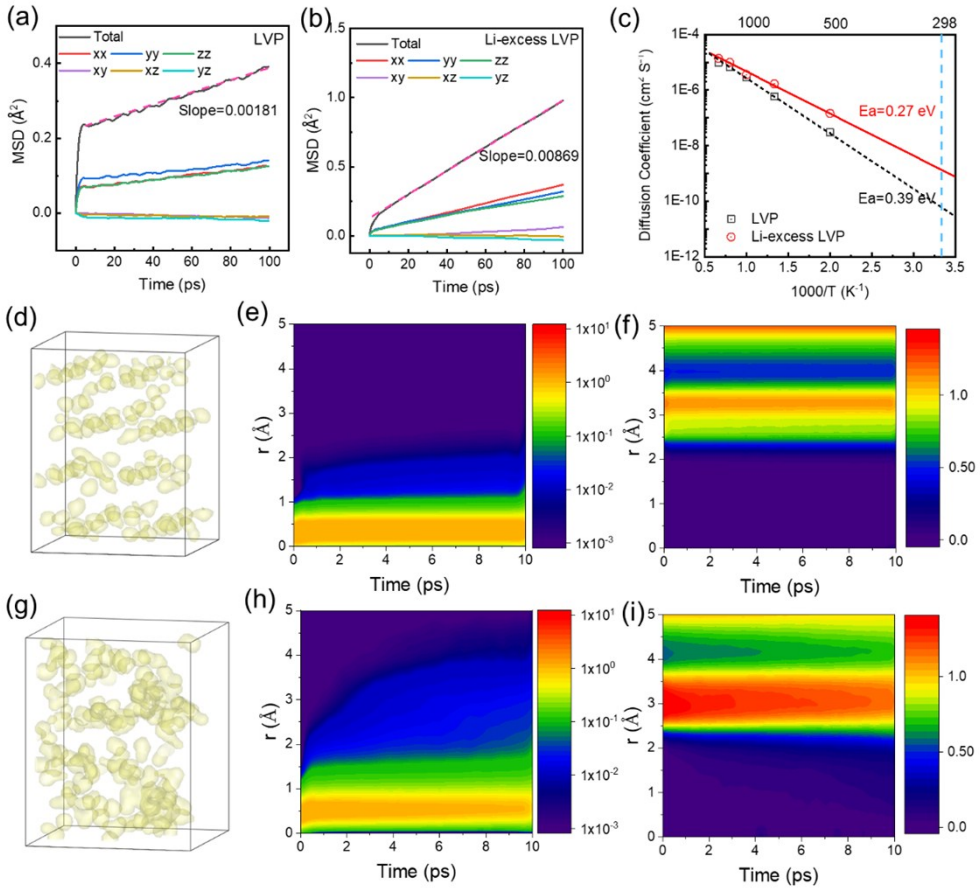

Figure S13 Li ion diffusion for normal and lithium-excess LVPs at 500 K: (a, b) The mean-squared displacement (MSD) functions. (c) Arrhenius plots and activation barriers for the lithium ion migration. (d, g) The probability density of Li-ion spatial occupancy during MD simulations, (e, h)

Self Van Hove correlation functions ($4\pi r^2 Gs$) of Li^+ dynamics, (f, i) Distinct Van Hove correlation functions (G_d) of Li^+ dynamics.

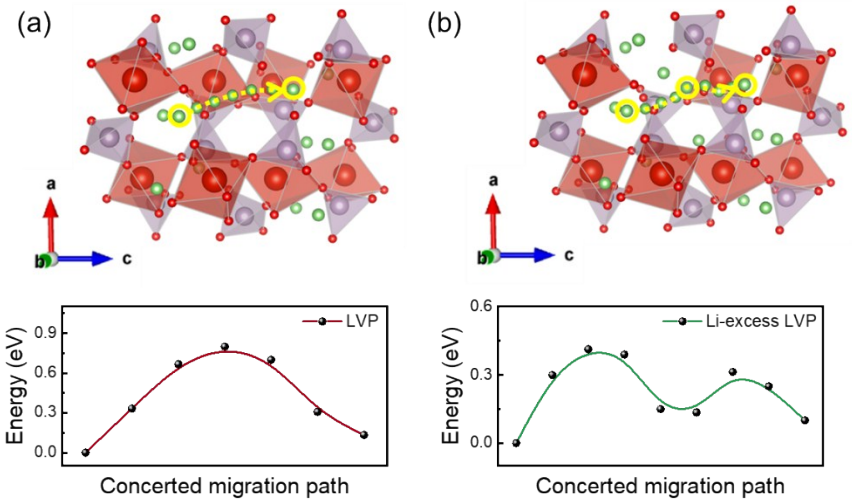

Figure S14 Migration activation energy of the Li^+ diffusing along with c-axis

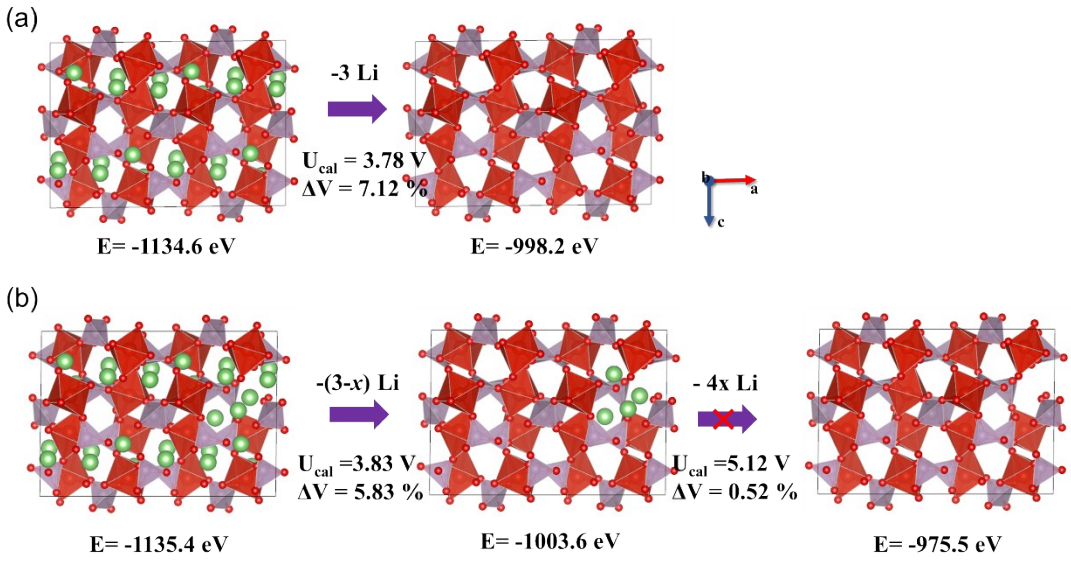

Figure S15 Schematic diagram of delithiation process of normal (a) and Li-excess (b) LVPs

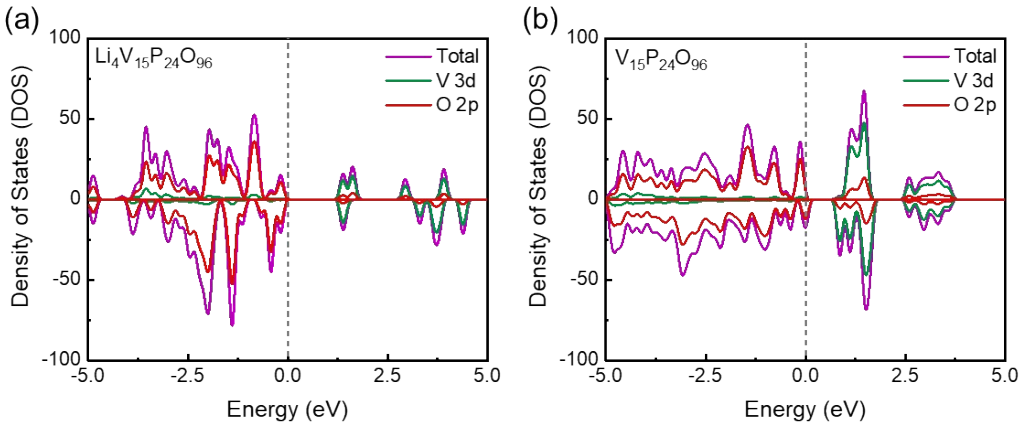

Figure S16 The PDOS of during delithiation process: (a) $Li_4V_{15}P_{24}O_{96}$, (b) $V_{15}P_{24}O_{96}$

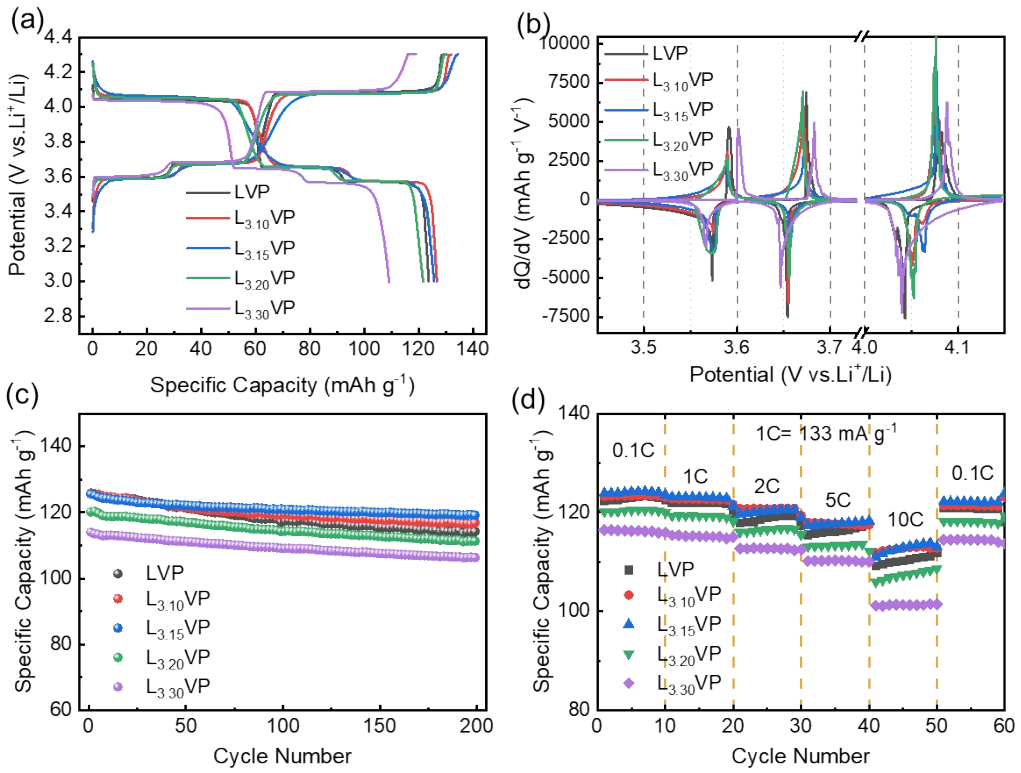

Figure S17 Electrochemical performances of LVP, $L_{3.05}VP$, $L_{3.10}VP$, $L_{3.15}V$ and $L_{3.20}VP$ at a potential range of 3.0-4.3 V: (a) galvanostatic charge-discharge profiles, (b) dQ/dV curves, (c) cycling performances at 0.5C rate and (d) rate capabilities.

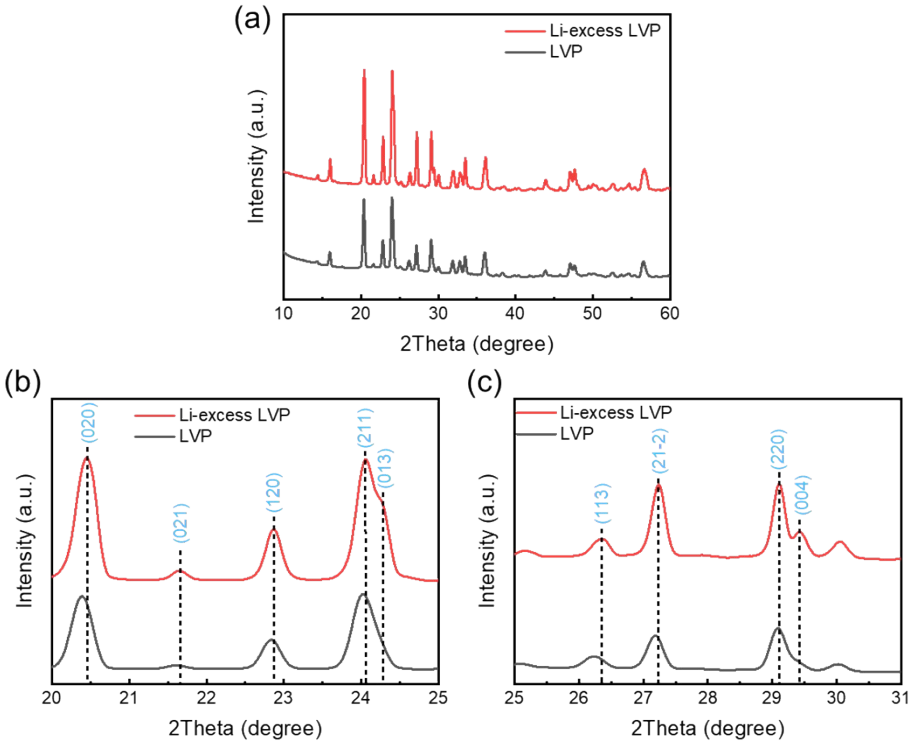

Figure S18 XRD patterns of normal and Li-excess LVPs after 100 cycles

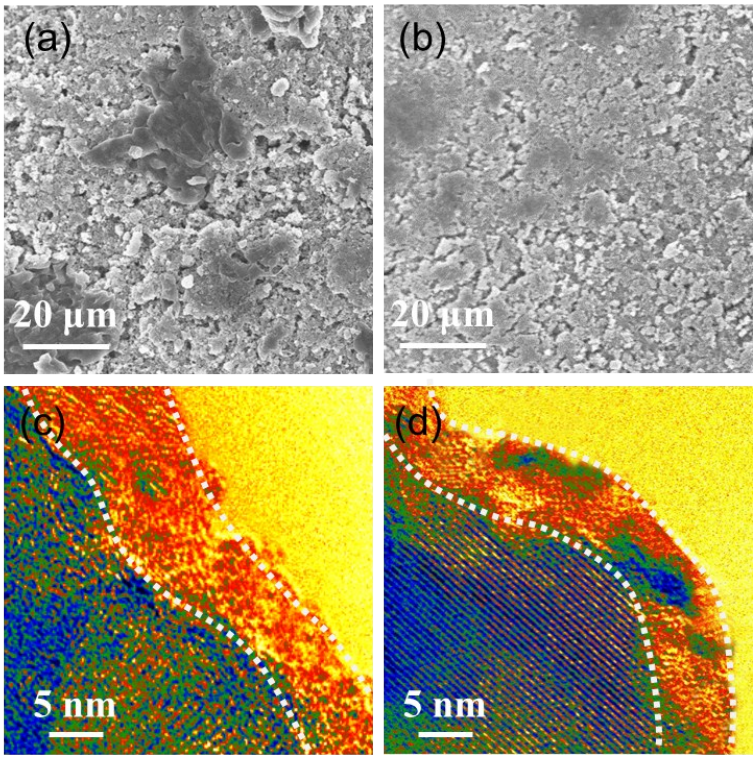

Figure S19 SEM and TEM images of normal LVP (a, c) and Li-excess LVP (b, d) after 100 cycles

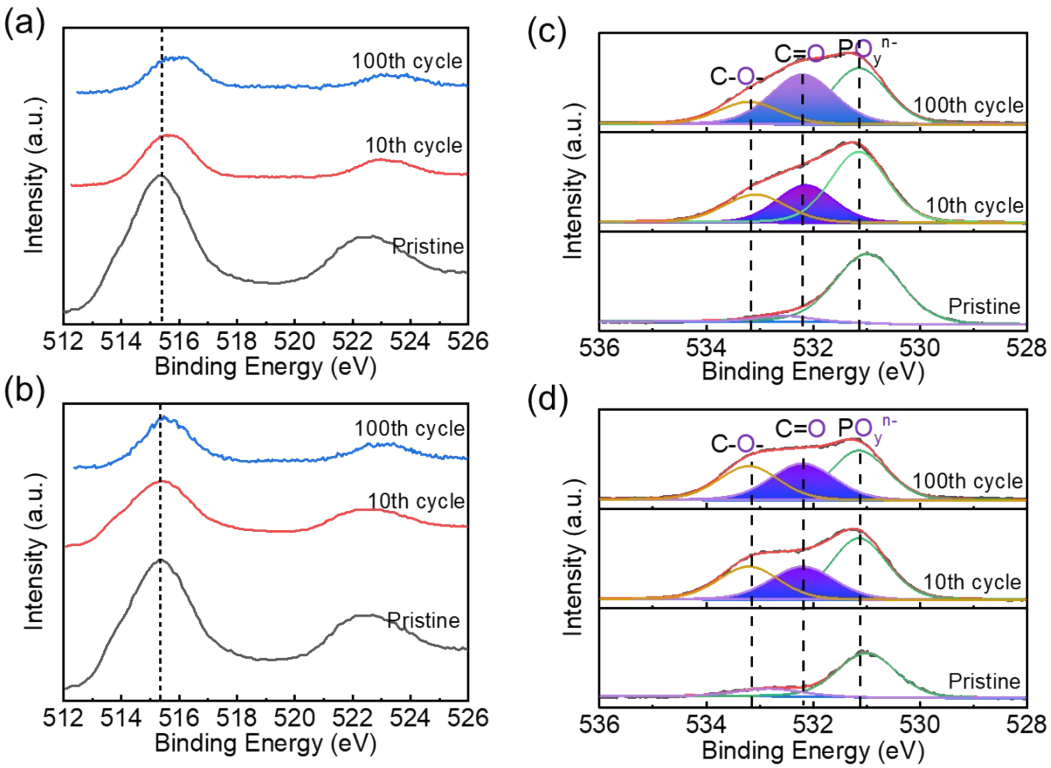

Figure S20. V 2p (a, b) and O 1s (c, d) XPS spectra of normal and Li-excess LVP at 1st, 10th and 100th cycle.

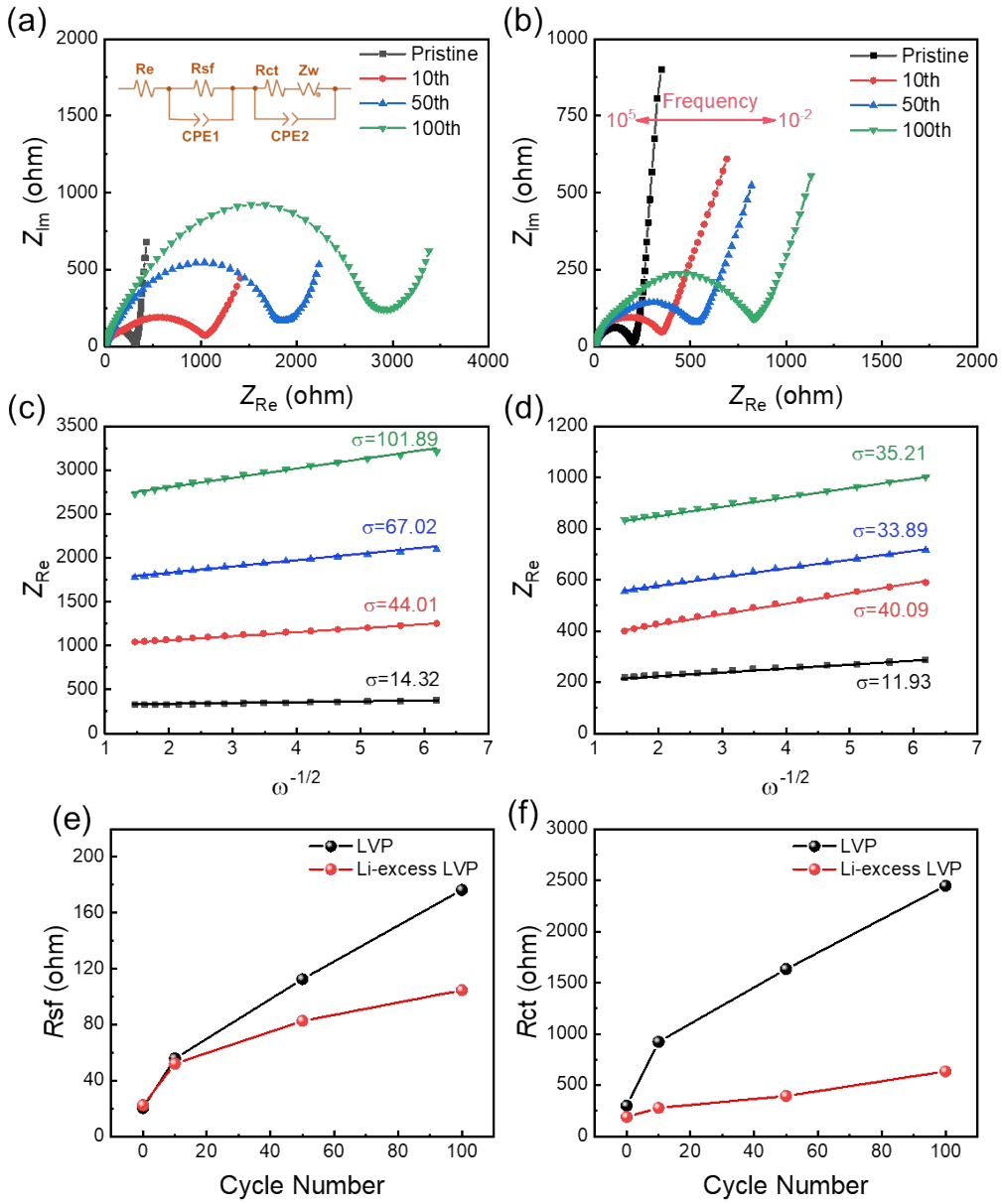

Figure S21 (a, b) EIS response of normal and Li-excess LVPs during cycling. (c, d) fittings between Z_{re} and the reciprocal square root of the angular frequency in the low frequency region. (e, f) The fitting values of R_{sf} and R_{ct} change.

The change of Li ion diffusion coefficient during cycling could be calculated based on Warburg impedance coefficient using (1) and (2).

$$Z_{Re} = R_e + R_{sf} + R_{ct} + \sigma_w \omega^{-1/2} \qquad (1)$$

$$D_{Li} = R^2T^2/2A^2n^4F^4C\sigma_w{}^2 \qquad (2)$$

where D_{Li} represents the lithium ion diffusion coefficient, R is the gas constant, T is the absolute temperature, A is the effective area of the electrode, n is the number of electrons transferred, F is Faraday constant, and C is the concentration of lithium ions. The Warburg impedance coefficient σ_w is determined from the slope of Z_{Re} as a function of $\omega^{-1/2}$.

Table S1. Calculated Formation Energies of Relevant Compounds in the Li-V-P-O_2 system

Compound	Space group	Formation Energies (eV f.u.$^{-1}$)
Li_2O	Fm3m	-6.10
Li_2O_2	$P6_3/mmc$	-6.60
Li_3PO_4	Pnma	-22.14
Li_3VO_4	$Pnm2_1$	-20.11
$Li_4P_2O_7$	$P2_1/c$	-35.85
$LiPO_3$	$P2_1/c$	-13.59
$LiV(PO_3)_4$	Pbcn	-48.38
$Li_3V_2(PO_4)_3$	$P2_1/c$	-54.78
$LiVP_2O_7$	$P2_1$	-30.21
$V(PO_3)_3$	Cc	-34.64
V_2O_3	Cmcm	-12.67
V_3O_5	P2/c	-20.19
VO_2	$P4_2/mnm$	-7.45
VPO_4	Pnma	-16.25
$LiVPO_5$	Pnma	-21.44
V_2PO_5	$I4_1/amd$	-20.88
$V_{12}P_7$	P6	-15.96

Table S2 Elemental composition and phase analysis and powder electronic conductivity of various Li-excess composition

Samples	Li : V : P	Phases	Electronic conductivity (10^{-4} S cm^{-1})
$L_{3.30}VP$	3.315 : 1.886 : 3	$Li_3V_2(PO_4)_3$, Li_3PO_4 (5.40 wt.%)	3.96
$L_{3.20}VP$	3.203 : 1.904 : 3	$Li_3V_2(PO_4)_3$, Li_3PO_4 (3.05 wt.%)	4.25
$L_{3.15}VP$	3.162 : 1.956 : 3	$Li_3V_2(PO_4)_3$	4.39
$L_{3.10}VP$	3.098 : 1.971 : 3	$Li_3V_2(PO_4)_3$	4.58
LVP	2.994 : 1.988 : 3	$Li_3V_2(PO_4)_3$	4.02

Table S3. Fitting results of V L-edge XANES spectra

Samples	Signal	Position (eV)	FWHM (eV)	Area	t_{2g}/e_g	dx^2-y^2/dz^2
LVP	A	513.71	1.6	0.3296	0.196	0.821
	B	515.01	1.15	0.7545		
	C	516.52	1.58	0.9188		
$L_{3.15}VP$	A	513.51	1.54	0.3501	0.217	1.719
	B	515.04	1.19	1.0164		
	C	516.55	1.37	0.5913		
$L_{3.20}VP$	A	513.54	1.15	0.3119	0.172	1.290
	B	515.02	1.23	1.0241		
	C	516.52	1.39	0.7941		

Table S4. polyhedral structural parameters for normol and Li-excess LVPs

V1-O_6	Distance (Å)	2.019	2.018	2.027
	Distortion index (Å)	0.017	0.015	0.015
	Bond angle variance (deg ^{2})	41.321	43.752	51.257
V2-O_6	Distance (Å)	2.026	2.028	2.037
	Distortion index (Å)	0.024	0.026	0.027
	Bond angle variance (deg ^{2})	42.993	44.149	61.753
P1-O_4	Distance (Å)	1.5403	1.547	1.541
	Distortion index (Å)	0.005	0.015	0.014
	Bond angle variance (deg ^{2})	14.451	21.361	26.172
P2-O_4	Distance (Å)	1.543	1.544	1.549
	Distortion index (Å)	0.008	0.006	0.011
	Bond angle variance (deg ^{2})	7.577	8.654	5.151
P3-O_4	Distance (Å)	1.541	1.542	1.541
	Distortion index (Å)	0.012	0.012	0.008
	Bond angle variance (deg ^{2})	25.022	24.672	13.918

Table S5 The CV peak features of various L_xVP/C samples

Samples	LVP	$L_{3.10}$VP	$L_{3.15}$VP	$L_{3.20}$VP	$L_{3.30}$VP
C1	3.633	3.658	3.635	3.659	3.655
C2	3.712	3.719	3.714	3.725	3.743
C3	4.155	4.141	4.136	4.133	4.162
C4	4.650	4.614	4.612	4.609	4.682
D1	3.898	3.901	3.903	3.866	3.729
D2	3.619	3.621	3.636	3.615	3.484
D3	3.560	3.561	3.571	3.556	3.484

References:

1. A. Jain, Y. Shin and K. A. Persson, *Nat Rev Mater*, 2016, **1**, 15004.
2. U. Maitra, R. A. House, J. Somerville, N. Tapia-Ruiz, J. G. Lozano, N. Guerrini, R. Hao, K. Luo, L. Y. Jin, M. A. Perez-Osorio, F. Massel, D. M. Pickup, S. Ramos, X. Y. Lu, D. E. McNally, A. V. Chadwick, F. Giustino, T. Schmitt, L. C. Duda, M. R. Roberts and P. G. Bruce, *Nat Chem*, 2018, **10**, 288-295.
3. A. Castets, D. Carlier, K. Trad, C. Delmas and M. Menetrier, *J Phys Chem C*, 2010, **114**, 19141-19150.
4. K. Momma and F. Izumi, *J Appl Crystallogr*, 2008, **41**, 653-658.
5. T. Bamine, E. Boivin, F. Boucher, R. J. Messinger, E. Salager, M. Deschamps, C. Masquelier, L. Croguennec, M. Menetrier and D. Carlier, *J Phys Chem C*, 2017, **121**, 3219-3227.
6. M. Sale and M. Avdeev, *J Appl Crystallogr*, 2012, **45**, 1054-1056.
7. S. Lee and S. S. Park, *The Journal of Physical Chemistry C*, 2012, **116**, 25190-25197.
8. X. F. He, Y. Z. Zhu and Y. F. Mo, *Nat Commun*, 2017, **8**, 15893.
9. Y. Deng, C. Eames, B. Fleutot, R. David, J. N. Chotard, E. Suard, C. Masquelier and M. S. Islam, *Acs Appl Mater Inter*, 2017, **9**, 7050-7058.
10. K. Y. Park, I. Park, H. Kim, G. Yoon, H. Gwon, Y. Cho, Y. S. Yun, J. J. Kim, S. Lee, D. Ahn, Y. Kim, H. Kim, I. Hwang, W. S. Yoon and K. Kang, *Energ Environ Sci*, 2016, **9**, 2902-2915.
11. W. J. Xiao, C. Xin, S. B. Li, J. S. Jie, Y. Gu, J. X. Zheng and F. Pan, *J Mater Chem A*, 2018, **6**, 9893-9898.